

## Prediction of Convective Initiation and Storm Evolution on 12 June 2002 during IHOP\_2002. Part I: Control Simulation and Sensitivity Experiments

HAIXIA LIU AND MING XUE

*Center for Analysis and Prediction of Storms, and School of Meteorology, University of Oklahoma, Norman, Oklahoma*

(Manuscript received 30 January 2007, in final form 16 August 2007)

### ABSTRACT

The 12–13 June 2002 convective initiation case from the International H<sub>2</sub>O Project (IHOP\_2002) field experiment over the central Great Plains of the United States is simulated numerically with the Advanced Regional Prediction System (ARPS) at 3-km horizontal resolution. The case involves a developing mesoscale cyclone, a dryline extending from a low center southwestward with a cold front closely behind, which intercepts the midsection of the dryline, and an outflow boundary stretching eastward from the low center resulting from earlier mesoscale convection. Convective initiation occurred in the afternoon at several locations along and near the dryline or near the outflow boundary, but was not captured by the most intensive deployment of observation instruments during the field experiment, which focused instead on the dryline–outflow boundary intersection point.

Standard and special surface and upper-air observations collected during the field experiment are assimilated into the ARPS at hourly intervals in a 6-h preforecast period in the control experiment. This experiment captured the initiation of four groups of convective cells rather well, with timing errors ranging between 10 and 100 min and location errors ranging between 5 and 60 km. The general processes of convective initiation are discussed. Interestingly, a secondary initiation of cells due to the collision between the main outflow boundary and the gust fronts developing out of model-predicted convection earlier is also captured accurately about 7 h into the prediction. The organization of cells into a squall line after 7 h is reproduced less well.

A set of sensitivity experiments is performed in which the impact of assimilating nonstandard data gathered by IHOP\_2002, and the length and interval of the data assimilation are examined. Overall, the control experiment that assimilated the most data produced the best forecast although some of the other experiments did better in some aspects, including the timing and location of the initiation of some of the cell groups. Possible reasons for the latter results are suggested. The lateral boundary locations are also found to have significant impacts on the initiation and subsequent evolution of convection, by affecting the interior flow response and/or feeding in more accurate observation information through the boundary, as available gridded analyses from a mesoscale operational model were used as the boundary condition. Another experiment examines the impact of the vertical correlation scale in the analysis scheme on the cold pool analysis and the subsequent forecast. A companion paper will analyze in more detail the process and mechanism of convective initiation, based on the results of a nested 1-km forecast.

### 1. Introduction

During the warm season over the Southern Great Plains (SGP) of the United States, strong convective storms are responsible for a large portion of the annual rainfall. Accurate prediction of quantitative precipitation associated with these warm-season systems has been a particularly elusive task (Fritsch and Carbone

2004). The prediction of the exact timing, location, and intensity of convective initiation and the subsequent evolution of the convective systems are even more difficult. Such difficulties arise in part from the poor knowledge of four-dimensional water vapor distribution with high temporal and spatial variability, inadequate understanding of the convective initiation (CI) processes, and the inability of typical numerical models to accurately represent important physical processes. To address some of these questions, the International H<sub>2</sub>O Project (IHOP\_2002; Weckwerth et al. 2004) field experiment was carried out in the spring of 2002.

Weckwerth and Parsons (2006) present a review on

---

*Corresponding author address:* Dr. Ming Xue, Center for Analysis and Prediction of Storms, National Weather Center, Suite 2500, 120 David L. Boren Blvd., Norman, OK 73072.  
E-mail: mxue@ou.edu

convective initiation, in particular, that caused by surface boundaries prevalent in the SGP environment. Wilson and Roberts (2006) systematically summarize all CI events and their evolution during the IHOP period, based on observational data. The ability of the operational 10-km Rapid Update Cycle (RUC; Benjamin et al. 2004) in predicting these events is also briefly discussed. Xue and Martin (2006a,b, hereafter XM06a and XM06b, respectively) present a detailed numerical study on the 24 May 2002 dryline CI case.

In XM06a,b, the Advanced Regional Prediction System (ARPS; Xue et al. 2000, 2001, 2003) and its data assimilation system were employed to simulate the events at 3- and 1-km horizontal resolutions. Accurate timing and location of the initiation of three initial convective cells along the dryline are obtained in the model at the 1-km resolution. Through a detailed analysis on the model results, a conceptual model is proposed in which the interaction of the finescale boundary layer horizontal convective rolls (HCRs) with the mesoscale convergence zone along the dryline is proposed to be responsible for determining the exact locations of convective initiation. Worth noting in this case is that the CI did not occur at the intersection point between the dryline and a southwest–northeast-oriented surface cold front located in the north, or at the dryline–cold front “triple point,” which conventional wisdom would highlight as the location of highest CI potential. In fact, most of the observing instruments were deployed around the triple point that day, missing the true CI that actually occurred farther south along the dryline.

Another CI event that was extensively observed during IHOP\_2002 is that of 12 June 2002, which also involved a dryline intersecting a cold front. Further complicating the situation was a cold pool and the associated outflow boundary that ran roughly east–west and intercepted both cold front and dryline near its west end. In the afternoon of 12 June, CI occurred along and near the dryline, and along and near the outflow boundary. Some of these storm cells organized into a squall line into the evening and propagated through the central and northeast part of Oklahoma through the night, producing damaging wind gusts, hail, and heavy precipitation. On this case, Weckwerth et al. (2008) performed a detailed observation-based study that employed multiple datasets and discussed preconvective, clear-air features and their influence on convective initiation. This case is also one of the two highlighted in the survey study of Wilson and Roberts (2006). Because of the limitations of the observational datasets, the CI mechanisms of this case could only be hypothesized in these two observation-based studies. For the same case, Markowski et al. (2006) analyzed the “con-

vective initiation failure” in a region near the intersection of the outflow boundary and dryline. Data from multiple mobile Doppler radars were used in their analysis. This region was chosen for intensive observations because of its proximity to the outflow boundary–dryline intersection point (similar to a triple point) but the actual initiation occurred about 40 km to the east and to the south along the dryline. Clearly, a better understanding of the CI mechanisms in this and other cases, and improvement in NWP model prediction skills, is needed.

In this study, a similar approach to that employed in XM06a,b is used to study the CI processes and subsequent storm evolutions in the 12 June 2002 case. Additional numerical experiments are also conducted to evaluate the impact of various model and data assimilation configurations. As in the study of XM06a,b, 3- and 1-km horizontal resolution grids are used, and the results of this study will be presented in two parts. In this first part (Part I), an overview of the case is presented, together with a brief description of the numerical model and its configurations, and of the data assimilation method and observation data used. This part will focus on the results of the 3-km grid, and examine, through a set of sensitivity experiments, the impact of a number of model and data assimilation configurations on the prediction of CI and storm evolution. In the second part of this paper (M. Xue and H. Liu 2008, unpublished manuscript, hereafter Part II), a detailed analysis of the results of the 1-km grid will be presented, with the primary goal of understanding the exact processes responsible for the CI.

The rest of this paper is organized as follows. In section 2, we discuss the synoptic and mesoscale environment of the 12 June 2002 case, the sequence of storm initiations along the dryline and the outflow boundary, and the subsequent evolution of these cells and their eventual organization into a squall line. Section 3 introduces the numerical model used and its configurations, as well as the design of actual experiments. The results are presented and discussed in sections 4 and 5 and a summary is given in section 6.

## 2. Overview of the 12 June 2002 case

As pointed out in the introduction, the case of 12 June 2002 is a complicated one that involves a number of mesoscale features that interact with each other. Figure 1 shows the surface observations superposed on visible satellite imagery at 2045 UTC or 1445 LST 12 June 2002 in the IHOP domain. There was an outflow left behind by a mesoscale convection system (MCS) earlier that day, located over southern Kansas (KS),

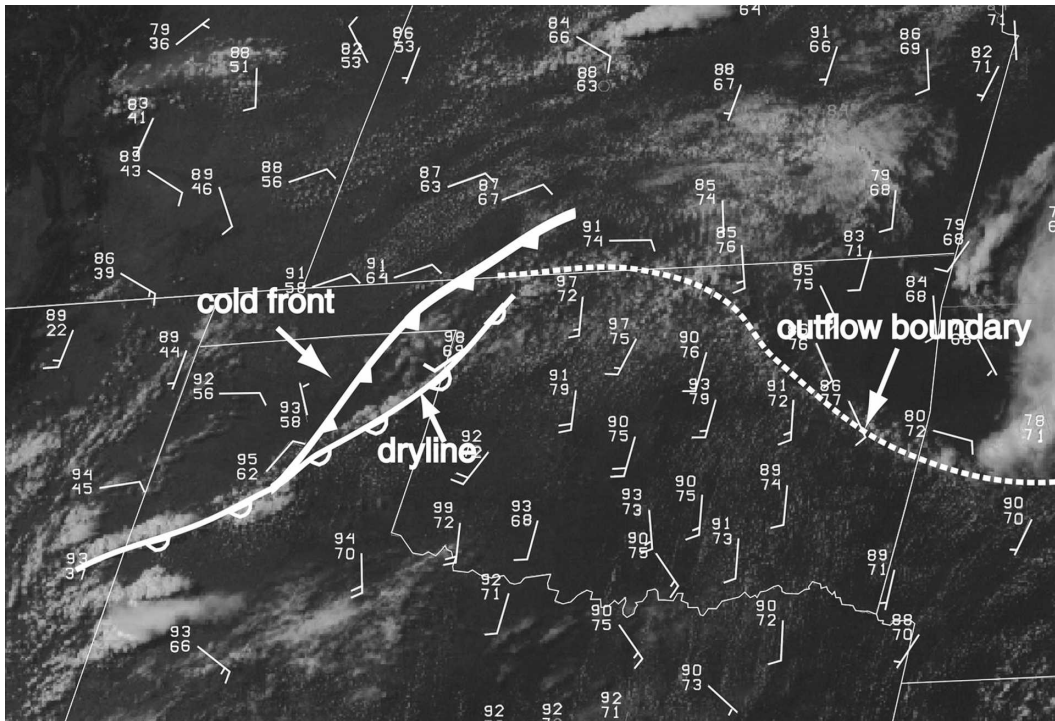


FIG. 1. Visible satellite imagery at 2045 UTC 12 Jun 2002, with surface observations overlaid. Station models show wind barbs (one full barb representing approximately  $5 \text{ m s}^{-1}$ ), and temperature and dewpoint temperature ( $^{\circ}\text{F}$ ).

northeastern Oklahoma (OK), and northwest Arkansas (AR). The southern boundary of this outflow (indicated by the dashed line in Fig. 1) stretched from far northwest OK to the northwest AR, separating the warm, moist, generally southerly flow to its south from the cool, but moist, easterly and southeasterly flow to the north of the boundary. During the day, this boundary receded to the north, acting more like a warm front. A weak cold front extended from the eastern OK Panhandle (at the western end of the outflow boundary) toward the south-southwest to the central Texas (TX) Panhandle. A dryline was present at the same time, oriented northeast–southwest from the eastern OK Panhandle to the southwestern TX Panhandle and intersected the cold front at the central TX Panhandle (at the southern end of the cold front). Warm dry air existed west of the dryline and ahead of the cold front where southwesterly winds dominated. Behind the cold front, most of the winds came from the north or north-northeast. The low-level winds showed the existence of a mesoscale cyclone west of the dryline–outflow boundary triple point (see, e.g., Fig. 4d). Another feature worth pointing out is a region east of the dryline with generally southerly surface winds exceeding  $7.5 \text{ m s}^{-1}$ , which provided ample moist air for CI near the dryline and outflow boundary.

Figure 2 shows the multiradar mosaic of composite (vertical column maximum) reflectivity as produced by the procedure of Zhang et al. (2005) at 2130, 0000, 0100, and 0300 UTC, which are the times when most storms were initiated, and when the squall line was organizing, intensifying, and maturing, respectively. The first group of convective cells in Fig. 2 was initiated at about 1900 UTC near the TX–New Mexico (NM) border (denoted 1a in Fig. 2a). One hour later (2000 UTC), the second cell group (denoted as 1b in Fig. 2a) was initiated 100 km north of group 1a. Group 1a was ahead of the dryline while group 1b was right over the southern extent of the dryline. During the next 40 min, more convective cells (denoted as 1c in Fig. 2a) were initiated near these two groups. At about 2030 UTC, near the intersection of the cold front and dryline near Amarillo, TX, another group of convective cells (denoted as 2 in Fig. 2a) was initiated and intensified quickly, leading to hail reports and strong winds along their gust fronts. During the next hour, additional convective cells formed, along the northern extent of the dryline (denoted as group 3) and near, but south of, the outflow boundary (denoted as group 4). Farther east along the outflow boundary, group 5 is found which was initiated at around 2000 UTC (Fig. 2a). By 0000 UTC 13 June (Fig. 2b), these cells reorganized into somewhat differ-

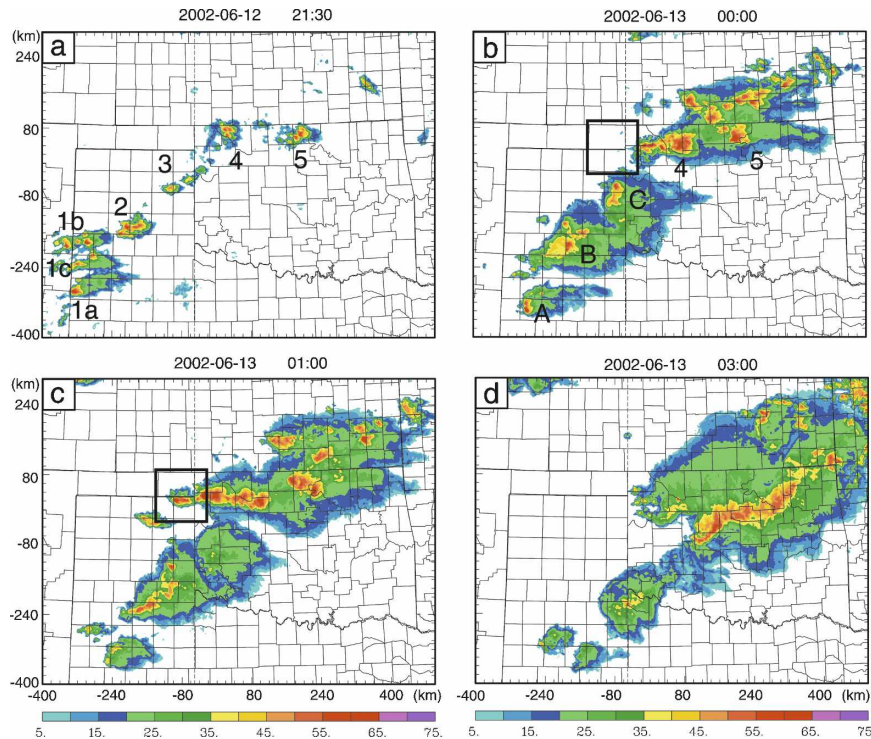


FIG. 2. Observed composite reflectivity mosaic at (a) 2130 UTC 12 Jun 2002, (b) 0000, (c) 0100, and 0300 UTC 13 Jun 2002. The letters 1a, 1b, 1c, 2, 3, and 4 mark the CI locations. The black squared box in (b) and (c) corresponds to the small zoomed-in domain shown in Fig. 8.

ent cell groups, denoted as A, B, C, 4, and 5. Group A is basically the group evolved from 1a, and B is a combination of groups 1b, 1c, and the southern part of 2 that underwent splitting during the period. Group C was made up of the northern part of 2 and 3 while groups 4 and 5 maintained their identities. Between 2130 and 0000 UTC, more cells developed north of the OK–KS border (Fig. 2b). During the hour after 0000 UTC, cell groups A, B, and C either weakened or nearly dissipated, while group 4 extended farther westward into the eastern OK Panhandle and group 5 grew in size (Fig. 2c). In the next 2 h, groups 4 and 5, together with other cells between them and farther to the east, became connected and organized into a solid squall line (Fig. 2d), which continued its propagation southeastward for the next 3 h until around 0600 UTC. The more detailed processes involved in the cell initiation and evolution will be discussed in the next two sections, together with the model simulations of these processes.

### 3. Numerical model, data, and experiment design

As in XM06a,b, version 5 of ARPS (Xue et al. 2000, 2001, 2003) is used in this study. The ARPS is a non-hydrostatic atmospheric prediction model formulated

in a generalized terrain-following coordinate. As in XM06a,b, two one-way nested grids at 3- and 1-km horizontal resolutions, respectively, are used. In the vertical, the grid spacing increases from about 20 m near the ground to about 800 m near the model top that is located about 20 km above sea level. The 3-km resolution is believed to be high enough to resolve important mesoscale structures, while 1-km resolution is necessary to resolve smaller convective structures, including many of the boundary layer horizontal convective rolls and individual cells of deep moist convection.

The model terrain and land surface characteristics on the 3- and 1-km grids are created in the same way as in XM06a,b. The lateral boundary conditions (LBCs) for the 3-km grid are from time interpolations of 6-hourly National Centers for Environmental Prediction (NCEP) Eta Model analyses and the 3-h forecasts in-between the analyses, while the 1-km grid gets its LBCs from the 3-km forecasts at 10-min intervals. In this study, the results of numerical simulations are found to be sensitive to the lateral boundary locations of the 3-km grid, and the domain of the 3-km grid used in our control simulation (see Fig. 3) is much larger than that used in XM06a,b. The impact of the domain size and boundary locations will be specifically discussed in section 5c.

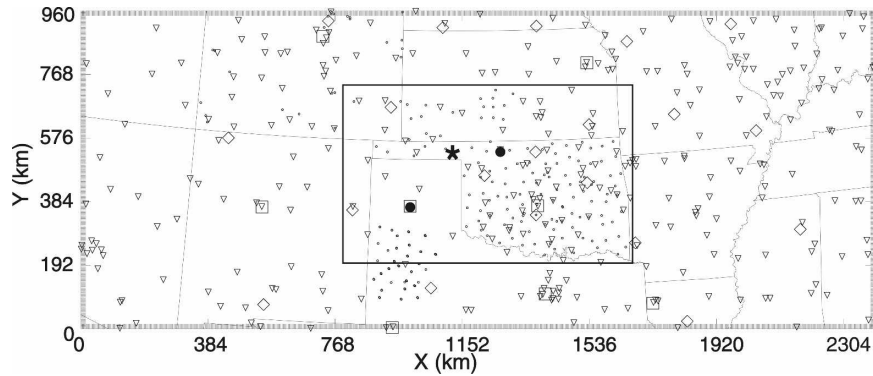


FIG. 3. The 3-km model domain used by all experiments except for SML, which uses the smaller domain shown by the rectangle in the figure. The stations of the Oklahoma Mesonet, the West Texas Mesonet, the southwest Kansas mesonet, the Kansas groundwater management district #5 network, and the Colorado agricultural meteorological network are marked by small dots; the stations of the ASOS and the FAA SAO are marked by downward triangles; the stations from the NWS radiosonde network are marked by squares; and the stations from the NOAA wind profiler network are marked by diamonds. Two filled circles mark the locations of KVNIX and KAMA WSR-88D radars in Oklahoma and Texas, respectively. The filled star represents the S-Pol radar station.

The ARPS is used in its full physics mode (see Xue et al. 2001, 2003). The 1.5-order (turbulent kinetic energy) TKE-based subgrid-scale turbulence parameterization and TKE-based PBL-mixing parameterization (Sun and Chang 1986; Xue et al. 1996) are used. The microphysics scheme is the Lin et al. (1983) three-ice microphysics. The National Aeronautics and Space Administration (NASA) Goddard Space Flight Center (GSFC) long- and shortwave radiation package (Chou 1990, 1992; Chou and Suarez 1994) is used and the land surface condition is predicted by a two-layer soil-vegetation model initialized using the state variables presented in the Eta analysis.

The initial conditions of our numerical simulations are created using the ARPS Data Analysis System (ADAS; Brewster 1996), in either the cold-start mode where the analysis is performed only once using an Eta analysis as the background, or with intermittent assimilation cycles where ARPS forecasts from the previous forecast cycles are used as the background for the cycled analyses. For all experiments to be presented, the initial conditions, created with or without assimilation cycles, are valid at 1800 UTC 12 June, about 1 h preceding the first observed convective initiation near the dryline. As one of the intensive observation days of IHOP\_2002 with convective initiation study as the mission goal, various remote sensing instruments were deployed on that day, in addition to routine and special conventional observations (Weckwerth et al. 2004). In this study, conventional forms of data are assimilated into the model initial condition, including those of (regular and mesonet) surface stations, upper-air

soundings, and wind profilers. Available aircraft data [i.e., the Meteorological Data Collection and Reporting System (MDCRS)] are also included. Table 1 lists the standard and special datasets used, together with their key characteristics. Figure 3 marks most of the observation sites used in this study. Data from the IHOP-deployed National Center for Atmospheric Research (NCAR) S-band polarimetric (S-Pol) radar and from the Weather Surveillance Radar-1988 Doppler (WSR-88D) radars in the region are used extensively for verification, especially KVNIX (Enid, OK) and KAMA (Amarillo, TX) radars (see Fig. 3).

After an initial condition is obtained at 1800 UTC on the 3-km grid, the ARPS model is integrated for 9 h until 0300 UTC 13 June 2002, the mature time of the squall-line system. The 1-km grid forecast also starts at 1800 UTC, with the initial condition interpolated from the 3-km grid, and runs until the same ending time. As pointed out earlier, we will present only the results from 3-km experiments in this part (Part I). The results of 1-km grid experiments, together with detailed analyses on the convective initiation mechanisms, will be presented in Part II.

In addition to a control simulation, we perform a set of sensitivity experiments at 3-km resolution to examine the impact of intermittent data assimilation cycles and IHOP special data, the effect of vertical correlation scales used in the ADAS, and the effect of lateral boundary locations (Table 2). In all ADAS analyses, five analysis passes are performed, with each pass including different sets of data and using different spatial correlation scales. Table 3 lists the observations ana-

TABLE 1. List of the abbreviations of the observation networks used in this study and some of their characteristics.

Type of dataset	Abbreviation	Description	Temporal resolution	Special or standard	No. of stations
Upper-air datasets	RAOB	NWS radiosonde network	3 h	Data at 1200 UTC are standard, others are considered special	18 at 1200 UTC; 10 at 1500 and 1800 UTC
	WPDN	Wind Profiler Demonstration Network	1 h	Standard	20
	COMP*	Special composite dataset composed of many upper-air observing networks	1 h	Special	1
	MDCRS	NWS Meteorological Data Collection and Reporting System aircraft observations	1 h	Special	Varies
Surface datasets	SAO	Surface observing network composed of the ASOS and the FAA surface observing network	1 h	Standard	About 250
	COAG	Colorado Agricultural Meteorological Network	1 h	Special	29
	OKMESO	OK Mesonet	1 h	Special	About 125
	SWKS	Southwest Kansas Mesonet	1 h	Special	8
	GWMD	Kansas groundwater Management District #5 Network	1 h	Special	10
	WTX	West Texas Mesonet	1 h	Special	30

\* A description on the individual networks included in the composite can be found in Stano (2003).

lyzed and the correlation scales for the horizontal and vertical for each analysis pass used in all experiments unless otherwise noted. Using one more pass than in XM06a,b, the horizontal correlation scale starts at a value slightly larger than in XM06a,b, and ends at a value that is smaller. The vertical correlation scales are generally smaller than the corresponding ones used in XM06a,b. These correlation scales were chosen based on additional experiments performed after the study of XM06a,b for the 24 May 2006 case.

Table 2 lists all numerical experiments with abbreviated names and their descriptions. The control experiment, CNTL, includes the most data (Table 1). Standard and special IHOP observations are assimilated in hourly analysis cycles over a 6-h period that ends at 1800 UTC. CNTL is designed to capture the convective cell initiation and later evolution into a squall line. Among the other experiments, COLD uses a cold-start analysis for the initial condition; 3HRLY uses two 3-hourly assimilation cycles, while 6HRLY uses a single

TABLE 2. Table of numerical experiments and their characteristics. Here CI1a, CI2, CI3, and CI4 refer to the convective initiation near the southwest most portion of the dryline, near Amarillo, TX, the intersection of cold front and dryline, and near Woods, OK, near the intersection of outflow boundary and dryline, corresponding to cell groups 1a, 2, 3, and 4, respectively.

Expt	Assimilated data	Assimilation interval	CI1a	CI2	CI3	CI4
			Time of CI in model and position error			
CNTL	All data	1 h	2040 UTC, 40 km SW	2040 UTC, <5 km	2250 UTC, 60 km NE	2130 UTC, 20 km NE
COLD	All data	Single analysis at 1800 UTC	Missing	Missing	2120 UTC, <10 km	Missing
3HRLY	All data	3 h	2030 UTC, 40 km SW	2040 UTC, <5 km	2200 UTC, 70 km NE	2050 UTC, 15 km NE
6HRLY	All data	6 h	2030 UTC, 60 km SW	2100 UTC, <5 km	2140 UTC, 70 km NE	2050 UTC, 50 km NE
STDOBS	Standard data only	1 h	2050 UTC, 40 km SSW	2030 UTC, 10 km E	2140 UTC, <10 km	2040 UTC, 5 km E
ZRANGE	All data	1 h	2030 UTC, 100 km SW	2000 UTC, <5 km	2220 UTC, 70 km NE	2100 UTC, 5 km N
SML	All data	1 h	1940 UTC, 10 km N	2010 UTC, 10 km NE	2240 UTC, 70 km NE	2110 UTC, 20 km N
Time of observed initiation			1900 UTC	2030 UTC	2130 UTC	2100 UTC

TABLE 3. List of analyzed observations and the horizontal and vertical correlation scales used by each pass of the ADAS analysis in all experiments except for ZRANGE.

Pass No.	Analyzed observations	Horizontal filter length scale (km)	Vertical filter length scale (m)
1	RAOB, WPDN, COMP, and MDCRS	320	500
2	RAOB, WPDN, COMP, MDCRS, and SAO	160	100
3	SAO, COAG, OKMESO, SWKS, WTX, and GWMD	80	100
4	SAO, COAG, OKMESO, SWKS, WTX, and GWMD	50	50
5	COAG, OKMESO, SWKS, WTX, and GWMD	30	50

6-hourly cycle. STDOBS includes only standard observations, as listed in Table 2, while ZRANGE tests the impact of different vertical correlation scales used in ADAS, and SML tests the impact of lateral boundary locations.

The performance of forecasts is evaluated by comparing the timing and location of the initiation of convective cells along and near the dryline and the outflow boundary against radar observations. The structure and evolution of the model storms and their later organization into a squall line are examined by comparing predicted and observed reflectivity fields. We realize that the verifications used here are mainly subjective. It is difficult to objectively evaluate the numerical forecast of convective initiation and its subsequent system evolution because of its spatial and temporal intermittency and its inherent predictability limit. Additional discussions on the use and limitation of ETS scores can be found in Dawson and Xue (2006), and in references cited therein.

#### 4. Results of the control experiment

Figures 4a–d show the analyzed surface fields of wind and water vapor mixing ratio during the 6-h assimilation cycle from 1200 to 1800 UTC for experiment CNTL. A dryline, as indicated by the strong moisture gradient, is well established during the period (Figs. 4b–d). Strong wind shift exists along the dryline. Figure 4e shows the analyzed surface temperature field and the mean sea level pressure at 1800 UTC. A mesoscale low center is found near eastern OK panhandle (marked by L). The MCS outflow boundary (thick dashed line in Fig. 4e) is indicated by the strong temperature gradient, and is accompanied by clear wind direction shift across the boundary (in Fig. 4d). Moisture is enhanced north of the boundary, especially near the central OK–KS border (Fig. 4d) and a strong cold pool is found at northeastern Oklahoma (Fig. 4e). To the south of the boundary and east of the dryline, strong southerly winds with speeds between 5 and 10  $\text{m s}^{-1}$  are found at the surface, with the strongest winds

being located in western OK and central TX and bringing rich moisture into the region, providing a favorable environment for CI and for the establishment of a squall line later on.

Figure 5 shows the temperature and wind vector fields at 850 hPa, which is close to the elevated ground in this panhandle region. The mesolow near the Oklahoma panhandle is clearly defined and the northerly flows west and southwest of the low center push forward a cold front, which is located behind the surface dryline (Figs. 1 and 4d). Significant small-scale structures exist in the surface moisture field, as indicated by the wiggles on the specific humidity contours (Fig. 4). These are related to the boundary layer (dry) convective structures that develop due to surface heating, and are generally of smaller scales than can be captured by the surface observation networks. In fact, such details are absent in the single-time analysis of the cold-start experiment COLD (Table 2), and most of the gradients are also weaker in that analysis (not shown).

In general, the prediction of convective initiation in CNTL is good. Figure 6 depicts the forecast fields of water vapor mixing ratio and winds at the surface, and the composite radar reflectivity at 2130 UTC 12 June 2002 and at 0000, 0100, and 0300 UTC 13 June, which can be compared directly to those in Fig. 2.

The model predicts the convective initiation at the intersection of the cold front and dryline near Amarillo, TX (denoted as 2 in Fig. 2a or CI2 in Table 2) remarkably well. The model convection is initiated around 2040 UTC and shows up as fully developed cells at 2130 UTC (marked by 2 in Fig. 6a). The location of this group of cells is almost exact and initiation timing error is about 10 min.

For the groups of cells denoted as 1a, 1b, and 1c in Fig. 2a, the situation is more complicated. In the real world, these cells were initiated over a period of about 1.5 h, starting at 1900 UTC, as described in section 2. The cells along the dryline, marked by 1b in Fig. 2a, were initiated around 2000 UTC. In the model, there are not three separate groups of cells as observed. A group of cells is initiated along the TX–NM border,

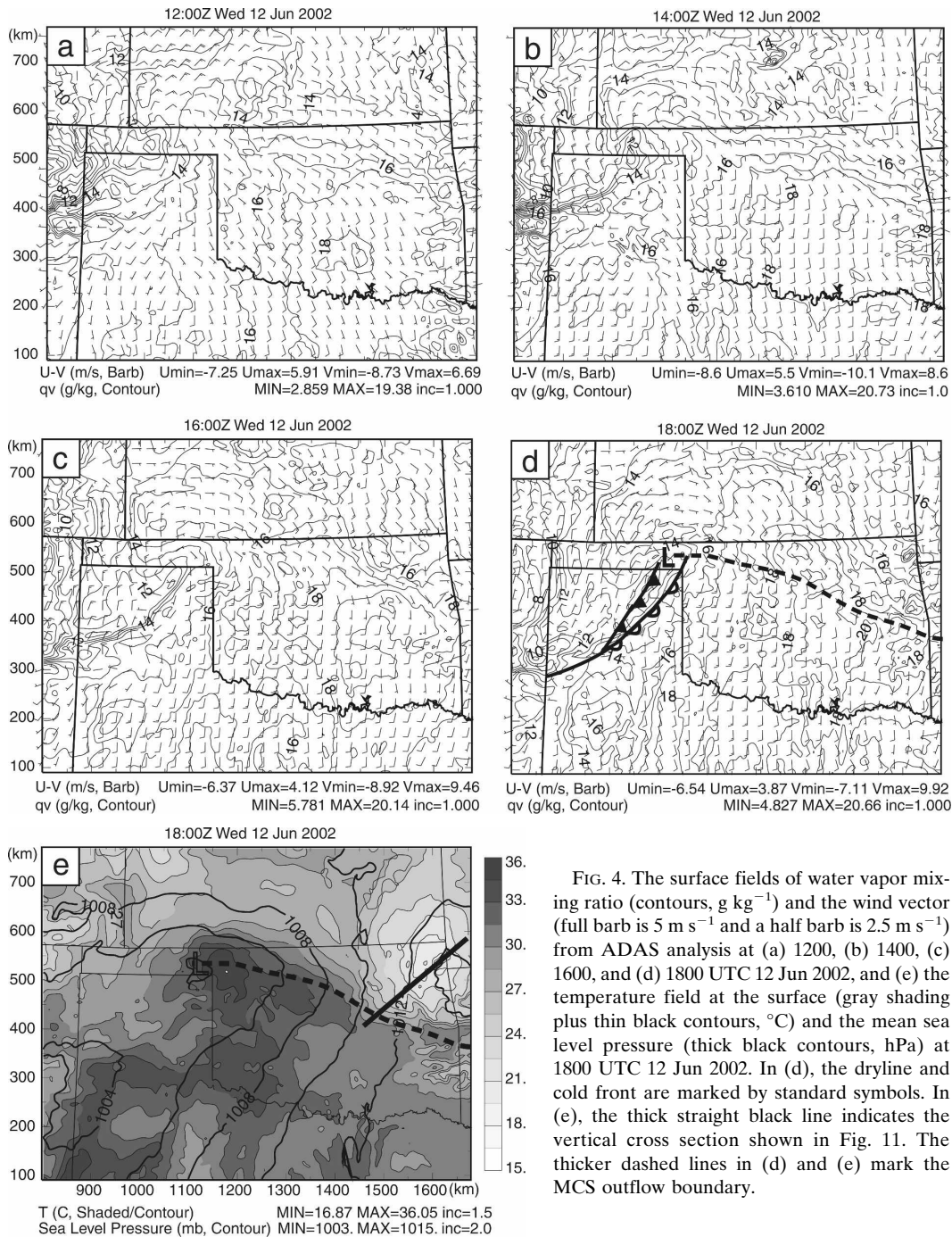


FIG. 4. The surface fields of water vapor mixing ratio (contours,  $\text{g kg}^{-1}$ ) and the wind vector (full barb is  $5 \text{ m s}^{-1}$  and a half barb is  $2.5 \text{ m s}^{-1}$ ) from ADAS analysis at (a) 1200, (b) 1400, (c) 1600, and (d) 1800 UTC 12 Jun 2002, and (e) the temperature field at the surface (gray shading plus thin black contours,  $^{\circ}\text{C}$ ) and the mean sea level pressure (thick black contours, hPa) at 1800 UTC 12 Jun 2002. In (d), the dryline and cold front are marked by standard symbols. In (e), the thick straight black line indicates the vertical cross section shown in Fig. 11. The thicker dashed lines in (d) and (e) mark the MCS outflow boundary.

south of the dryline at around 2040 UTC, at roughly the location of observed group 1a. At 2130 UTC (Fig. 6a), this group matches very well the observed cells in location (Fig. 2a). The cells associated with observed group 1b are much weaker in the model and are located farther east along the dryline, but still separate from observed cells 2 (Fig. 2a), especially as earlier times (not shown). Despite these discrepancies, the overall

behavior of model forecast in this region is still quite good.

Additional convective cells along the northern part of the dryline (group 3 in Fig. 2a) also develop in CNTL, but at a later time between 2240 and 2300 UTC (not shown) or about 1.5 h later than the observations. They are marked as “(3)” in Fig. 6a where the parentheses indicate that the cells do not yet exist at this time.

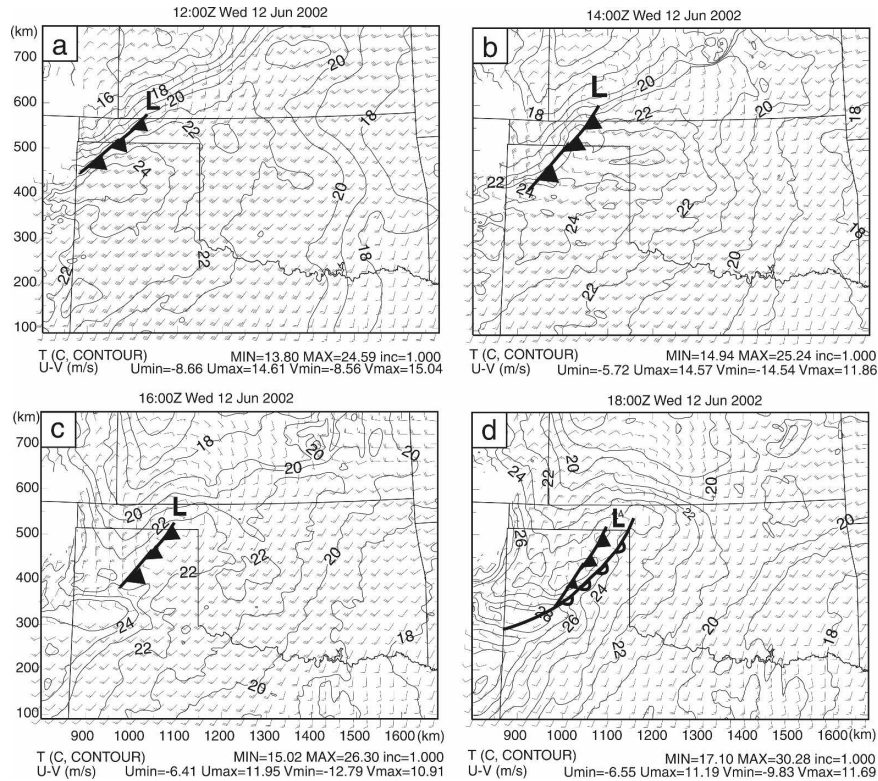


FIG. 5. The fields of temperature (contours, °C), and wind vectors (full barb = 5 m s<sup>-1</sup> and a half barb = 2.5 m s<sup>-1</sup>) at the 850-hPa level from ADAS analysis at (a) 1200, (b) 1400, (c) 1600, and (d) 1800 UTC 12 Jun 2002. (a)–(d) The cold front is marked by the standard symbol.

In the real world, part of cell group 2 merged with group 3 between 2130 and 0000 UTC to form the group marked by C in Fig. 2b, located on the west side of the western OK–TX border. In the model, a similar process occurs during this period and the model group “C” is located off to the east side of the same OK–TX border (Fig. 6b), giving rise to a location error of less than half a county or about 30 km.

In the model, a small cell starts to become visible at 2130 UTC (4 in Fig. 6a) that corresponds to the observed group 4 near the OK–KS border. The observed cell 4 had a similar intensity as this model cell in terms of radar echo at around 2110 UTC and reached 55-dBZ intensity by 2130 UTC (Fig. 2a); there is therefore a time delay of 20–30 min in the model with this cell. The model initiation occurs about 20 km northeast of the observed one. This cell does occur in the model to the south of the surface wind shift and convergence line and to the east of the dryline, as was observed by radar, which can identify the dryline and convergence line as reflectivity thin lines (not shown).

The evolution of the model predicted reflectivity pattern is similar to that observed. In the real world, cell group 2 split at around 2150 UTC, with the southern

part merging with groups 1b and 1c to eventually form group B and the northern part merging with group 3 to form group C (Fig. 2b). Group 1a remained by 0000 UTC 13 June (Fig. 2b). In the model, the splitting of group 2 starts to occur at around 2140 UTC with some sign of splitting visible at 2130 UTC (Fig. 6a); the northern part moves northeastward and merges with some much weaker cells in the model (model group 3) that develop along the northern portion of the dryline to form group C. Group C gains its maximum echo intensity of almost 70 dBZ near Amarillo at around 2330 UTC, the same time observed reflectivity reaches maximum intensity, then starts to weaken. By 0000 UTC, when it crosses the western OK border, it is already rather weak; it dissipated quickly afterward. Such an evolution is very similar to the observed one. As pointed out earlier, the peak intensity of the observed group C also occurs before 0000 UTC (the time of Fig. 2b), at around 2330 UTC.

In the model, the southern part of the split group 2 moves south-southeastward slowly and merges with the northeastward propagating group 1, at around 2350 UTC to form group B seen in Fig. 6b. This group then dies out gradually over the next 3 h (Figs. 6c,d).

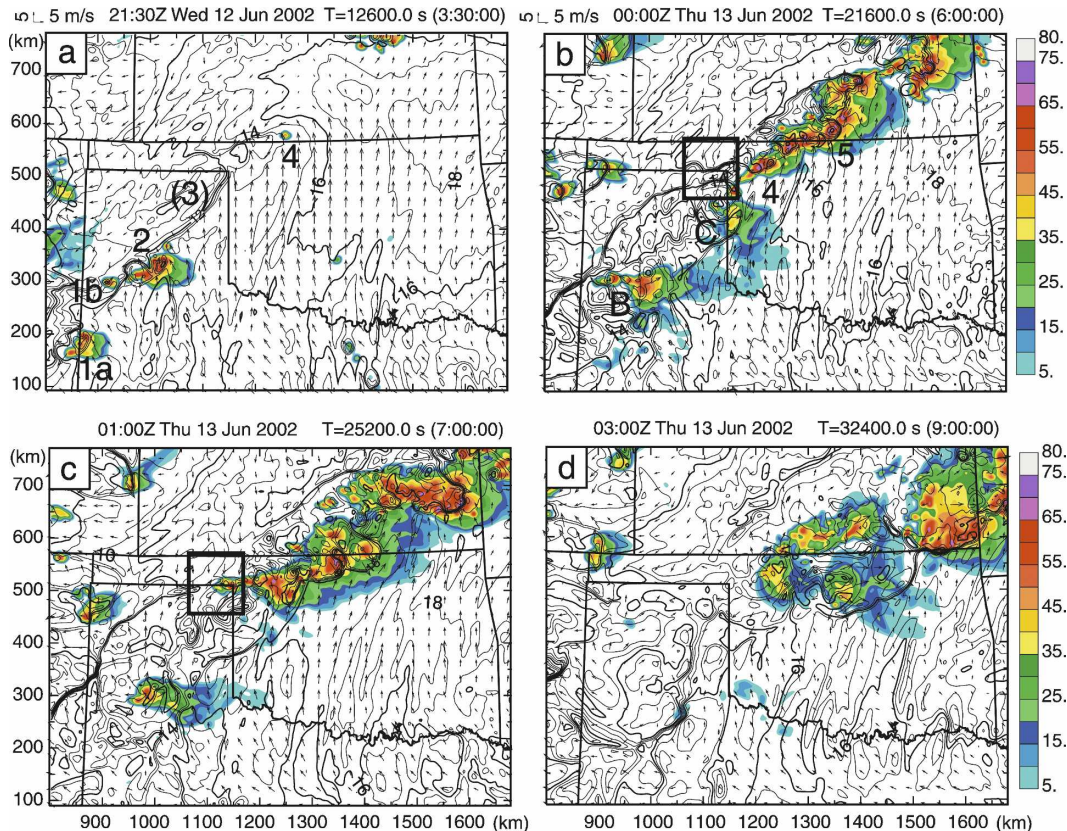


FIG. 6. The forecasted surface fields of water vapor mixing ratio (contour interval is  $1.0 \text{ g kg}^{-1}$ ), the wind vector ( $\text{m s}^{-1}$ ), and composite reflectivity (shaded, dBZ) at (a) 2130 UTC 12 Jun 2002, (b) 0000, (c) 0100, and (d) 0300 UTC 13 Jun 2002 from CNTL. Numbers 1, 2, and 4 in (a) indicate the locations of three primary convective cells. The black squared box in (b) and (c) corresponds to the small zoomed-in domain shown in Fig. 8.

Almost all cells that were initiated along the dryline dissipated by 0300 UTC 13 June, both in the real world (Fig. 2d) and in the model (Fig. 6d). The main development between 0000 and 0300 UTC 13 June occurred along the outflow boundary close to the OK–KS border, and the storm cells there eventually organized into a squall line by 0300 UTC (Fig. 2d). Actually, cell groups 4 and 5 found at 2130 UTC (Fig. 2a) represent the origin of the final organized squall-line system. These cells formed just south of (group 4) or along (group 5) the outflow boundary, and intensified (Fig. 2b) and merged with new cells that developed over the ensuing few hours near the convergence boundary, as well as with cells that formed east of the dryline in northwest OK before 0000 UTC. In the model, cell group 4 is found at a similar location as the observed counterpart at 0000 UTC (Fig. 6b) while the modeled group 5 is located farther north than the observed, and exists in the form of a connected line rather than more discrete cells. The group of cells in a northeast–southwest-oriented line north and northeast of group 5

seems to also match the observations well at this time. In the model, these cells apparently formed near the convergence boundary that had been pushed northward across the OK–KS border by the strong southerly flow. A similar development appears to have occurred in the real world too, based on more frequent radar maps (not shown).

By 0000 UTC, observed cell group 4 had already gained an elongated east–west orientation (Fig. 2b). During the next hour, this “line” extended westward by about 100 km (Fig. 2c) through the initiation of new cells. The initiation of these cells in a region behind the dryline was actually due to the collision between the original outflow boundary and the northwestward-propagating gust front from the earlier dryline convection. The tight water vapor contours in the square of Fig. 6b indicate the original MCS outflow boundary and the outflow boundary from dryline convection approaching each other, and they have collided by the time of Fig. 6c and triggered new convection. Such a process is most clearly seen in the low-level reflectivity

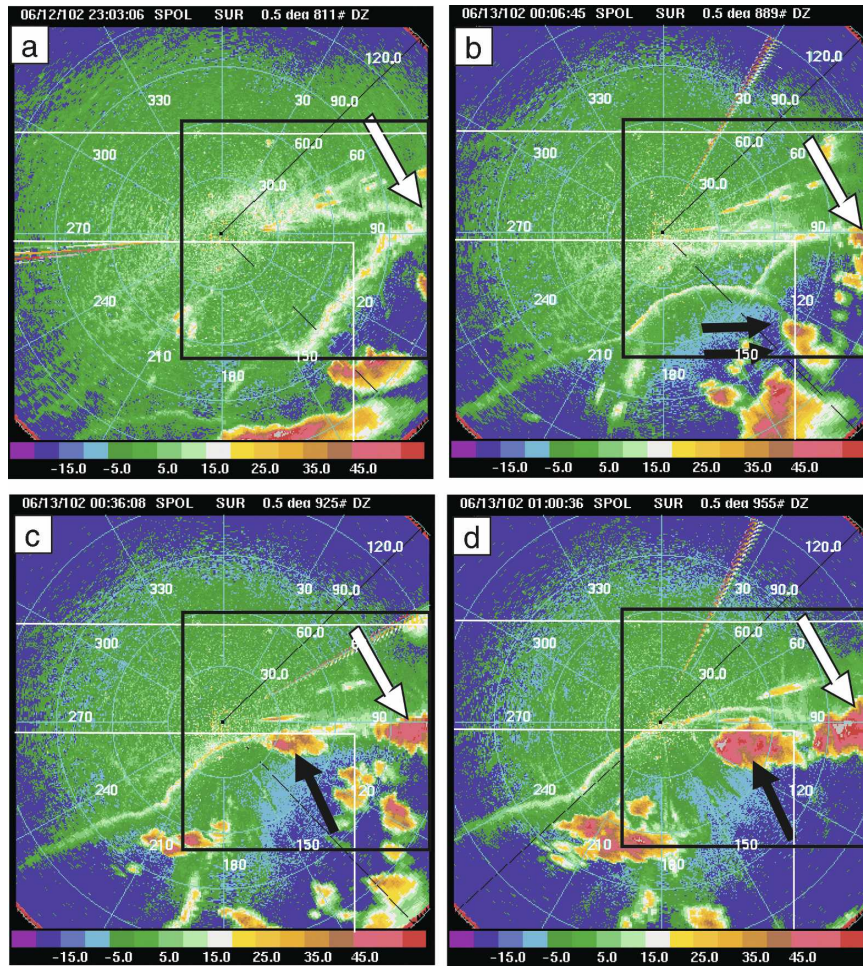


FIG. 7. The S-Pol radar reflectivity observations at 0.5° elevation angle at (a) 2303 UTC 12 Jun 2002, (b) 0006, (c) 0036, and (d) 0100 UTC 13 Jun 2002. The large black box in (a)–(d) indicates the domain shown in Fig. 8 and the arrows point to the locations of convective cells triggered by collisions of outflow boundaries. The radar range rings shown are for 30, 60, 90, and 120 km.

fields of the NCAR S-Pol radar deployed in the OK Panhandle during IHOP. In Fig. 7, the gust fronts and the convergence lines are seen clearly as thin lines with enhanced reflectivity. At 2303 UTC, two outflow boundaries are clearly visible (Fig. 7a) and by 0006 UTC, the eastern portion of the gust front, in a bow shape, has just collided with the northern outflow boundary (Fig. 7b), starting to produce new cells indicated by the large open arrow. The western, stronger, bow-shaped gust front was advancing and spreading rapidly and collided before 0006 UTC with the eastern bow-shaped gust front, producing a cell indicated by double solid arrows. By 0036 UTC, only 30 min later, this western portion has also collided with the northern outflow boundary, triggering and leaving a new cell right behind the gust front, as indicated by the large

black arrow (Fig. 7c). By 0100 UTC, this cell and the one formed earlier to the east (i.e., the two indicated by the two large arrows) reached their full strength and started to merge laterally (Fig. 7d).

Interestingly, almost exactly the same processes occurred in the model (Figs. 6b,c and 8). At 2300 UTC (Fig. 8a), the two predicted outflow boundaries as indicated by bold dashed lines, are seen to match the observed ones reasonably well (Fig. 7a). At 0000 UTC (Fig. 8b), the cell (indicated by double arrows) triggered by the two bow-shaped outflow boundaries are almost exactly reproduced, so are the shape and location of the three outflow boundaries. The cell indicated by the large open arrow also matches observation at this time. By 0030 UTC, the western portion of the northward advancing boundary has collided with the

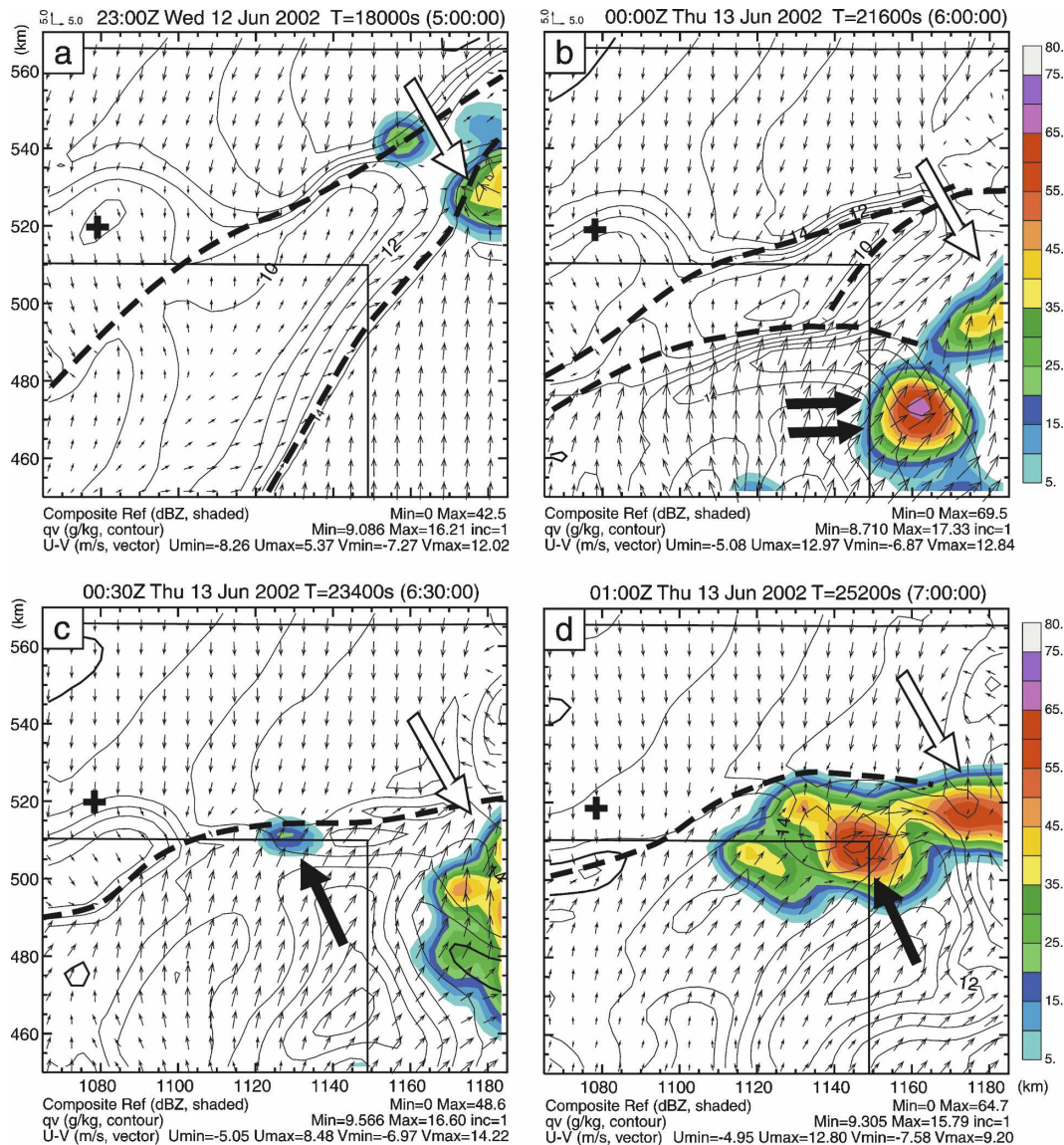


FIG. 8. As in Fig. 6, but for a zoomed-in region shown by the black squared box in Fig. 6b and for times (a) 2300 UTC 12 Jun 2002, (b) 0000, (c) 0030, and (d) 0100 UTC 13 Jun 2002, which are close to the times of NCAR S-Pol observations shown in Fig. 7. The plus sign indicates the location of the S-Pol radar. The arrows point to convective cells to be discussed in the text and the bold dashed lines indicate the outflow convergence boundaries.

northern one, and produced, as observed, a new cell, indicated by the large black arrow, and by 0100 UTC, this new cell as well as the eastern one intensified and the shape, intensity, and location of these two cells match the observations almost exactly (Figs. 8d and 7d). These cells became the westward extension of cell group 4 (Fig. 6c) as observed (Fig. 2c).

We should point out that in the same time period, a small cell developed in the observations in the lower-left corner of the black box (Figs. 7c,d). The same did not develop in the simulation, however. The reason for this discrepancy is not clear.

In the next 2 h from 0100 UTC, the model did not do a good job in organizing the cells into a squall line. The cells in group 4 that should have contributed to the western section of the squall line weakened subsequently and remained too far north, in northwest OK, while those that should make up the eastern section remained too far northeast, in the far southeast corner of KS (Fig. 6d). As will be shown in later sensitivity experiments, too strong southerly flow found in eastern OK is at least partly responsible for the dislocation of the eastern part of the squall line.

In summary, experiment CNTL presented above

which incorporated routine and special observations through hourly assimilation cycles successfully reproduced many of the observed characteristics of cell initiation in a complex mesoscale environment that involved an intensifying mesoscale low, a dryline, a cold front, as well as an outflow boundary resulting from an earlier mesoscale convective system. The predicted location and timing of most of the cells agree rather well with observations, with CI timing errors being only about 10 min and location errors being less than 5 km for the cell group near the intersection point of the dryline and cold front where mesoscale convergence forcing is strong. The secondary cell initiation due to the collision between the preexisting outflow boundary and the new gust front developing out of earlier dryline convection is also predicted very well by the model. The most significant problem is with the lack of organization of the cells into a solid squall line after 0010 UTC, or 7 h into the prediction. The difficulty in maintaining the position of the existing MCS outflow boundary to within northeastern Oklahoma in the model has contributed to this problem, which appears to be related to the too strong southerly flow in that region. This issue will be explored through a sensitivity experiment that attempts to better analyze the initial cold pool behind the outflow boundary and one that uses a different eastern boundary location, which results in a somewhat better flow prediction in eastern OK. Most importantly, the MCS precipitation is not reproduced in the model during the assimilation window, which is believed to be the main reason for the outflow to be quickly washed out during the forecast. Furthermore, the 3-km model resolution may have been inadequate for the cell interaction and organization. The impact of higher resolution will be examined in Part II. The results of sensitivity experiments will be presented in the following sections.

## 5. Results of sensitivity experiments

### *a. The impact of data assimilation length and frequency and the impact of special IHOP data*

For high-resolution convective-scale prediction, special issues exist for arriving at the optimal initial condition. At such scales, conventional observational data, including those from mesoscale surface networks, usually do not have sufficient resolution to define storm-scale features. Improper assimilation of such data can sometimes cause undesirable effects such as weakening the existing convection in the background and introducing unbalanced noise. The simulation reported in XM06a,b used only a single 6-hourly assimilation cycle, and no impact of data assimilation was examined in that

study. For the prediction of an isolated supercell storm event, Hu and Xue (2007) examined the impact of assimilation window length and assimilation intervals, for storm-scale radar data. The prediction results were found to be sensitive to the assimilation configurations.

Among all experiments presented in this paper, CNTL assimilates the most data (Table 2). Both standard and IHOP special observations (Table 1) are assimilated during a 6-h time window at hourly intervals. To examine the impact of assimilation interval, we perform additional experiments 3HRLY and 6HRLY, in which both standard and special observations are assimilated, but at 3- and 6-hourly intervals, respectively, over the same 6-h period (between 1200 and 1800 UTC). In addition, in the “cold-start” experiment COLD, a single analysis without assimilation cycle is performed at 1800 UTC.

Another experiment, called STDOBS (Table 2), was also performed, which is the same as CNTL except for the exclusion of special data collected by IHOP. Here, the surface data routinely available from the Automated Surface Observing System (ASOS) and the Federal Aviation Administration’s (FAA) surface observing network (SAO data in Table 1), and the NWS radiosondes available twice daily and the hourly wind profiler network data are considered standard data. All other data listed in Table 1 are considered special data, including special soundings taken at 1500 and 1800 UTC. For all cases, 9-h forecasts were performed, and the results are compared in terms of the prediction of CI and subsequent storm evolution.

Figure 9 shows the model predicted fields of composite reflectivity, surface water vapor mixing ratio, and wind vectors from COLD, 3HRLY, 6HRLY, and STDOBS, valid at 0100 UTC. It can be seen that the overall storm structure in COLD poorly matches the observed reflectivity shown in Fig. 2c (e.g., the convection in western TX is mostly missing) while those in the other three experiments match observations better, especially for the convection in northwest OK. However, unlike in CNTL, the initiation of new convection in eastern OK Panhandle due to the collision of outflow boundaries (cf. Fig. 6c) is missing in all of these experiments. In 6HRLY, the convection in western TX is overpredicted (cf. Figs. 9c and 2c), while in STDOBS, the convection is overall too strong. At the southwestern end of the overall system, the convection and the associated cold pool spread too far southeastward (Fig. 9d versus Fig. 2c), and the cold pool in northern OK and in KS appears to have also spread too far, creating two separate lines of cells along the gust fronts on its southeast and northwest sides. All other experiments predicted one dominant line of cells along the southern

01:00Z Thu 13 Jun 2002 T= 7:00:00

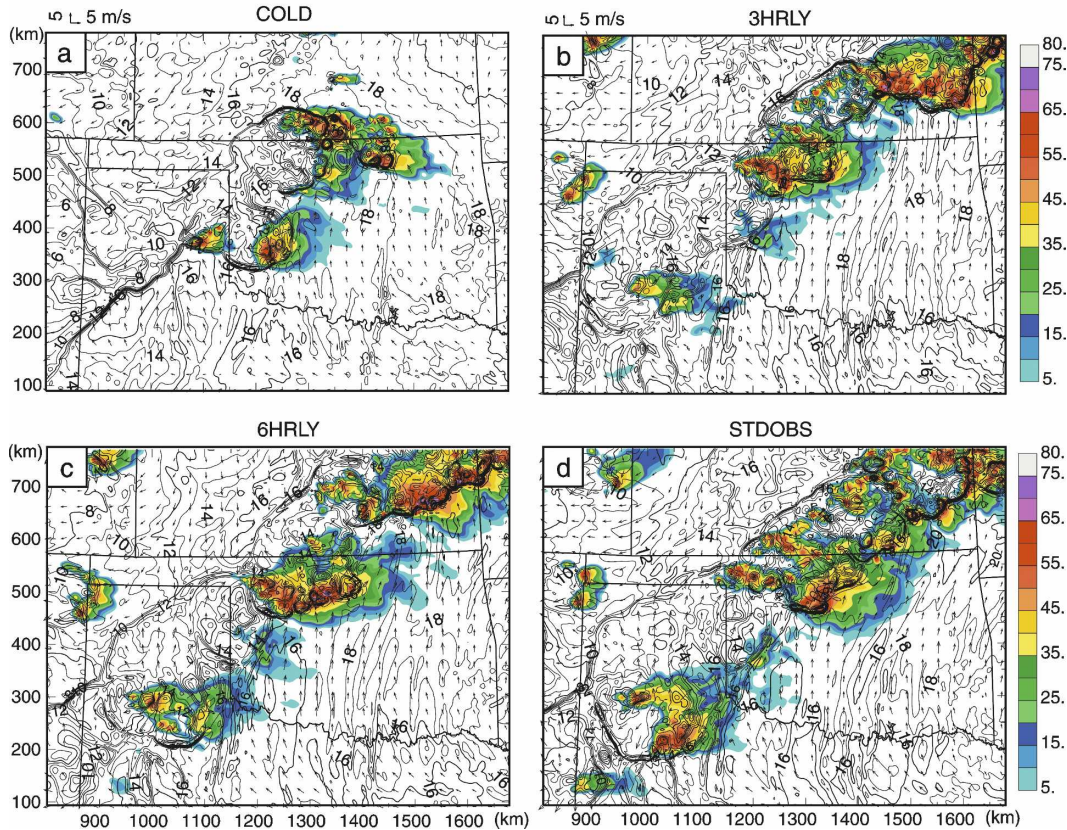


FIG. 9. As in Fig. 6c, but for experiments (a) COLD, (b) 3HRLY, (c) 6HRLY, and (d) STDOBS at 0100 UTC 13 Jun 2002.

gust front as observed. Overall, the prediction of CNTL matches the observation best, at least at this time.

Table 2 lists the timing and location errors of the four primary cell initiations (i.e., CI1a, CI2, CI3, and CI4), as compared against radar observations. Here the timing of convective initiation is determined as the time of first significant radar echo or reflectivity exceeding 30 dBZ. It can be seen that in most cases, the model CI tends to be delayed compared to observations. In the case of COLD, CI1a, CI2, and CI4 are completely missing. In all other cases listed in the table, the model was able to predict all four CIs, although with different degrees of accuracy. Among the five experiments (CNTL, COLD, 3HRLY, 6HRLY, and STDOBS), 3HRLY has the best timings for CI1a and CI4, STDOBS has the best timings for CI2 and CI3, while 6HRLY shares the best timing for CI3 with STDOBS, and for CI4 with 3HRLY. CNTL has timing accuracies for CI1a and CI2 similar to the other experiments, but has delay in the initiation of CI3 and CI4 (2250 versus observed 2130 UTC for CI3 and 2130 versus 2100 UTC for CI4). The other three experiments predict the initiation of CI4 somewhat ear-

lier instead. Overall, CI2 is best predicted; the presence of strong cold front–dryline forcing is probably the reason. The differences in the timing and location errors of CI1a among the successful experiments are also relatively small; again probably due to the strong dryline forcing.

Intuitively, experiment CNTL assimilated the most data, so the final analysis at 1800 UTC should be more accurate than those obtained using fewer data. We believe this is true for the analysis of mesoscale and synoptic scale features, including the dryline, outflow boundary, mesoscale low, and the broad flow pattern in general, as supported by the fact that the subsequent evolution of storms is predicted best in CNTL overall. Very frequent assimilation of mesoscale and synoptic-scale observations do not, however, necessarily improve the analysis of *convective-scale* features or flow structures that are resolved by the high-resolution model grid in the background forecast because of the insufficient spatial resolutions of such observations. In this case, the 3-km grid is able to resolve a significant portion of the *convective-scale* ascent forced by the

horizontal convergence of the developing dryline and the outflow boundary, and by boundary layer convective eddies and rolls (cf. XM06b). The analysis of mesoscale data, being of much coarser spatial resolutions (at  $\sim 30\text{--}100$  km), tends to weaken low-level horizontal convergence that develops in the model, hence weakening the forced ascent that is responsible for the triggering of convection.

A comparison between the domainwide maximum vertical velocity ( $w_{\max}$ ) before and after each analysis during the 6-h assimilation window indicates that the analyzed maximum vertical velocity is always smaller than that of the background forecast; that is, the analysis reduces small-scale upward motion. For example, in CNTL, the  $w_{\max}$  values before and after the analysis at 1800 UTC are about 12 and  $6.4 \text{ m s}^{-1}$ , respectively, and are about 13 and  $9.5 \text{ m s}^{-1}$ , respectively, at 1500 UTC. We believe that the reduced ascent is partly responsible for the delay of CI4 and northward displacement of cells (because of the farther northward retreat of the outflow boundary) in CNTL and in some of the other experiments, while the relatively coarse 3-km resolution is another major reason for the delay (Part II will show that the CI timing is much earlier when a 1-km grid is used). The dynamic consistency among the analyzed fields does not seem to be a major issue with the use of frequent hourly cycles.

The timing and location errors in STDOBS for CI1a and CI2 are similar to those of CNTL (Table 2). However, the predicted timing and location for CI3 and CI4 are better in STDOBS than in CNTL. For CI3, the timing error is only about 10 min (2140 versus 2130 UTC) and the location error is less than 10 km, while for CI4, the timing error is 20 min (2040 versus 2100 UTC) and the location error is less than 5 km. The prediction of these two CIs is much better than that of CNTL, which has a significant delay in both CIs. However, the prediction of the convective storm evolution at later times in STDOBS is not better than in CNTL as discussed earlier; there is a significant overprediction of convection at, for example, 0100 UTC (Fig. 9d).

Cell group 4 was initiated near the dryline–outflow boundary “triple” point, which was the focal point of intensive observation during IHOP\_2002. The actual initiation was to the southeast of the triple point, however. To better see how and why cell group 4 is initiated in the model, we plot in Fig. 10 the horizontal convergence (gray shading), specific humidity, temperature, and wind fields at the surface for CNTL, 3HRLY, 6HRLY, and STDOBS at their times of first cloud formation, for a small domain around CI4. The first cloud formation is determined as the time when the  $0.1 \text{ g kg}^{-1}$  contours of column maximum total condensate first ap-

pear within the plotting domain, which are shown as bold solid contours in the plots. Also overlaid in the plots are composite reflectivity contours for precipitation that first appear later on out of the initial clouds. We refer to such reflectivity as first echo. The times of first clouds are close to 2020, 2010, 2000, and 1950 UTC for CNTL, 3HRLY, 6HRLY, and STDOBS, respectively, while the corresponding times of first echo or CI are 2130, 2050, 2050, and 2040 UTC, as discussed earlier. The observed CI is at 2100 UTC. The maximum timing difference among the experiments is 30 min for first clouds and that for first echoes is 50 min.

The general surface flow patterns at the time of first cloud are similar between CNTL and STDOBS (Figs. 10a,d) while those of 3HRLY and 6HRLY are similar to each other (Figs. 10b,c). For CNTL and STDOBS, the lines of strong wind shift between southerly flow ahead of and the easterly or northeasterly flow behind the outflow boundary are located near the OK–KS border, in a east–west orientation, while those in 3HRLY and 6HRLY are in a more northeast–southwest orientation, located farther north. It is believed that the hourly assimilation cycles helped improve the low-level flow analyses in CNTL and STDOBS.

The wind shift or shear line corresponds to a zone of enhanced convergence. South of this shear line in the generally southerly flow, finescale convergence bands are clearly evident in all four experiments, with the orientation more or less parallel to the low-level winds. These bands are associated with boundary horizontal convective rolls and eddies that are resolvable by the relatively coarse 3-km resolution; the interaction of these bands can create localized convergence maxima that form preferred locations of convective initiation (XM06b). Apparently, in all four cases, the first cloud (indicated by the bold solid contours in Fig. 10) is found directly over or very close to the localized convergence maximum (spots of enhanced gray) that is closest to the warm and moist air coming from the south or southeast. The convergence maxima located farther west or north do not trigger convection as early or not at all because of lower values of low-level moisture and/or temperature there. We suggest that the wind shift line still played an important role in the convection initiation in this region, by providing a favorable environment with low-level mesoscale convergence.

The location of first cloud in CNTL almost exactly coincides with the observed first echo (marked by x in Fig. 10) while the first clouds in the other three experiments are located within 30 km of this location. The ensuing first echoes developed at different rates, with that in CNTL being the slowest (taking 70 min until 2130 UTC), and those in the others taking 40–50 min.

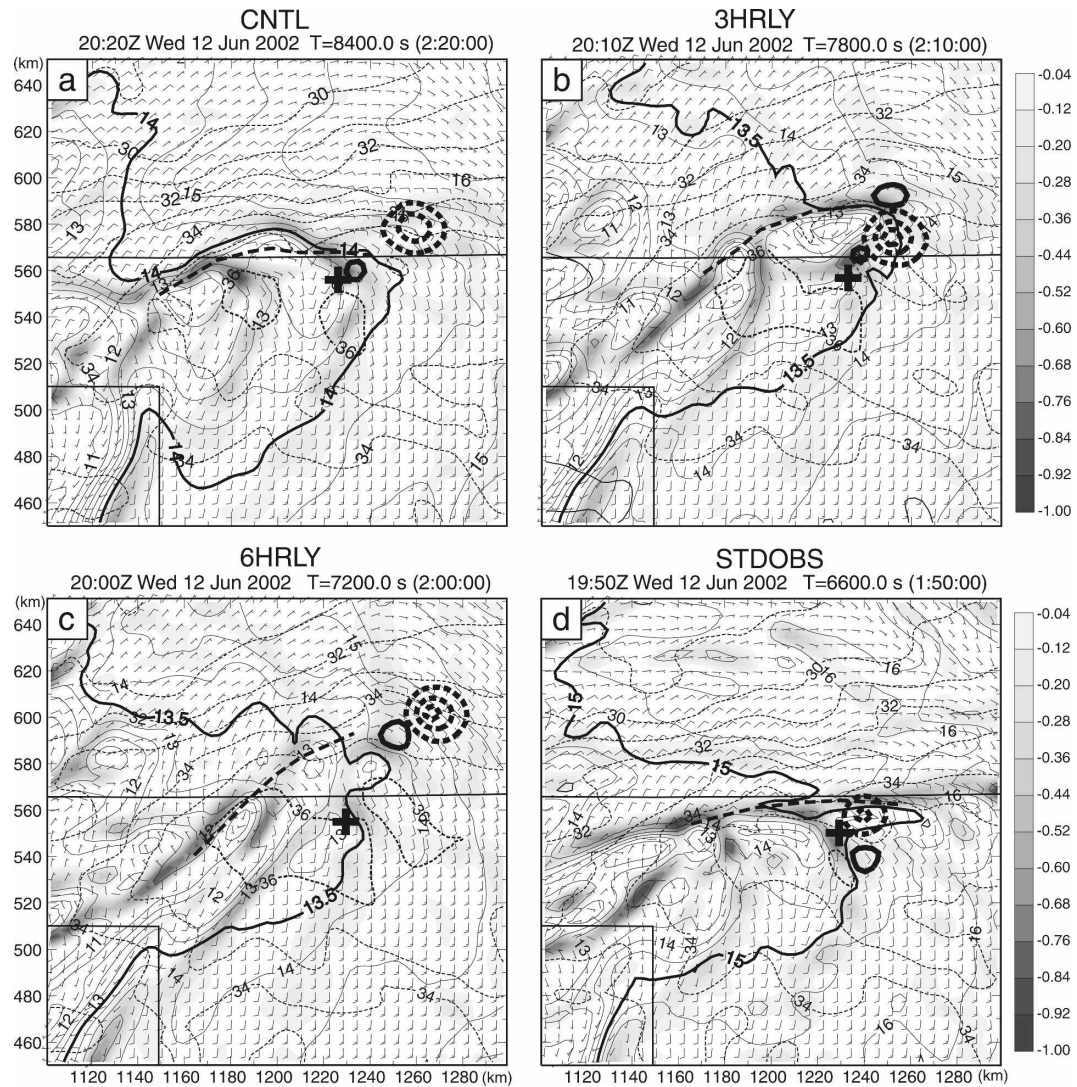


FIG. 10. Surface fields of horizontal divergence (only negative values shown in shaded gray), specific humidity [thin solid contours with 14, 13.5, 13.5, and  $15 \text{ g kg}^{-1}$  contours highlighted by thicker lines in (a), (b), (c), and (d), respectively], temperature (thin dashed contours with  $36^\circ\text{C}$  contours highlighted by thicker lines), and the  $0.1 \text{ g kg}^{-1}$  contour of total condensed water/ice (bold solid contours) for experiments (a) CNTL at 2020 UTC, (b) 3HRLY at 2010 UTC, (c) 6HRLY at 2000 UTC, and (d) STDOBS at 1950 UTC 12 Jun 2002, which correspond to the times of first cloud formation in the experiments. The bold dashed contours are for composite reflectivity (10-dBZ intervals starting at 10 dBZ) when it first appears out of the initial clouds at 2130, 2050, 2050, and 2040 UTC for the four experiments, respectively. The main wind shift or shear line associated with the outflow boundary is indicated by a thick dashed line in each plot. The location of observed CI4 is marked by a plus sign.

In CNTL, 3HRLY, and 6HRLY, the first echoes are found to the northeast of the corresponding first clouds, while that in STDOBS is found to the north of the first cloud. These relative locations indicate the direction of cloud and cell propagation, which is to a large degree controlled by the horizontal winds that advect them. The complexity of the first cloud formation and the subsequent development of the first echo, in terms of the location relative to the primary outflow boundary

convergence and maximum convergence centers due to boundary layer convective activities, suggest a degree of randomness. We leave the discussion about the exact processes of CI to Part II.

As discussed earlier, among experiments CNTL, 3HRLY, 6HRLY, and STDOBS, the initiation of CI4 occurred the earliest in STDOBS, at 2040 UTC, 20 min earlier than observed while that in CNTL occurred 30 min later than observed at 2130 UTC. Such timing dif-

ferences can be explained by the fact that the surface relative humidity at the time of first cloud is the highest in north-central OK in STDOBS (Fig. 10), which has values of around  $15 \text{ g kg}^{-1}$  in the region (Fig. 10d), while in other cases the values are between 13 and  $14 \text{ g kg}^{-1}$  (see the highlighted dark contours in the plots). The surface temperatures in the region are much closer, all around  $36^\circ\text{C}$ . Because CNTL, 3HRLY, and 6HRLY assimilate Oklahoma Mesonet data (Brock and Fredrickson 1993; Brock et al. 1995), which enjoy good data quality, surface analyses using them should be more reliable than that from STDOBS. Another reason that the low-level air of STDOBS is believed to be too moist is that there was some spurious light precipitation around 1800 UTC in STDOBS in southwestern OK (not shown); the advection of moistened air would result in higher low-level moisture in north-central OK. Therefore, the apparent better timing of CI4 initiation is not necessarily for the right reason.

*b. Effect of vertical correlation scales in ADAS on the analysis and prediction of the cold pool*

The outflow boundary created by the earlier MCS played an important role in this case, in helping initiate cell groups 4 and 5 and in the later organization of convection into a squall line. Earlier studies have shown the importance of properly initializing a cold pool for mesoscale prediction (Stensrud and Fritsch 1994; Stensrud et al. 1999). In our case, the ADAS is used to analyze the surface and other observations. The ADAS is based on the Bratseth (1986) successive correction scheme and analyzes observations using multiple iteration passes. The spatial correlation scales of observations are empirically specified and usually change with data sources and iterations (Brewster 1996). Theoretically, spatial correlation scales should be based on flow-dependent background error covariance but such covariance is generally unavailable at the mesoscale. Because the choice of correlation scales is empirical, the impact of the choices should be investigated. For the analysis of the cold pool, the vertical correlation scale is of particular interest.

The horizontal and vertical correlation scales used in CNTL and other experiments (except for ZRANGE) are listed in Table 3. The choice of these correlation scales is based on additional experiments performed after the study of XM06a,b, for the 24 May 2002 case that focuses on convective initiation along a dryline; these values differ somewhat from those used in XM06a,b. For the analysis of the cold pool behind the outflow boundary, the vertical scales ranging from 50 to 500 m used in CNTL appear too small for the surface data to properly reconstruct the cold pool, because too

shallow a cold pool results. In experiment ZRANGE, larger vertical correlation scales of 800, 400, 300, 200, and 100 m are used for the five successive passes. This results in a deeper vertical influence of surface observations and hence a deeper analyzed cold pool, as shown in Fig. 11 by the comparison of vertical cross sections from CNTL and ZRANGE, in northeast OK along a line roughly normal to the outflow boundary (as indicated in Fig. 4e). It is clear from Fig. 11 that the analyzed cold pool is deeper in ZRANGE (Fig. 11b versus Fig. 11a), and is maintained longer in the forecast, as seen from both of its depth and horizontal extent (Fig. 11c versus Fig. 11d and Fig. 11e versus Fig. 11f). The deeper cold pool in this region helped create a strong convergence farther west along the outflow boundary as the cold air is advected west-northwestward (cf. Fig. 4), resulting in a somewhat earlier and better timing of the initiation of cell group 4 (Table 2) than in CNTL.

However, this set of larger vertical correlation scales did not lead to a better prediction of the initiation of all of the other cell groups, nor of the general evolution of convection. This suggests that the increased vertical correlation scales do not necessarily improve the analysis in other regions outside the cold pool. For truly optimal analysis, flow-dependent background error correlation scales have to be estimated and used. Such flow-dependent statistics will require more sophisticated assimilation methods such as the ensemble Kalman filter (Evensen 1994).

*c. Impact of lateral boundary locations*

For limited-area simulation and prediction, the location of the lateral boundaries and the specification of lateral boundary conditions have a significant impact (Warner et al. 1997). In this study, the lateral boundary conditions are obtained from the Eta real-time analyses at 6-h intervals, and from interleaved 3-h forecasts. They are linearly interpolated to the model time and spatially interpolated to the 3-km resolution grid. In 2002, the horizontal resolution of the operational Eta forecasts was 12 km and the data used in this study had been interpolated to a 40-km grid with 39 pressure levels before downloading from NCEP. For the experiments reported earlier, a rather large computational domain, as shown in Fig. 3, is used. This choice is based on some initial experiments where sensitivity to the lateral boundary location was found. In this subsection, some of the sensitivities of CI and later evolution of convection to the boundary location are documented.

In our case, there exists a significant low-level flow response to the daytime heating over the sloping terrain in the TX Panhandle area. Between 1200 and 1800 UTC,

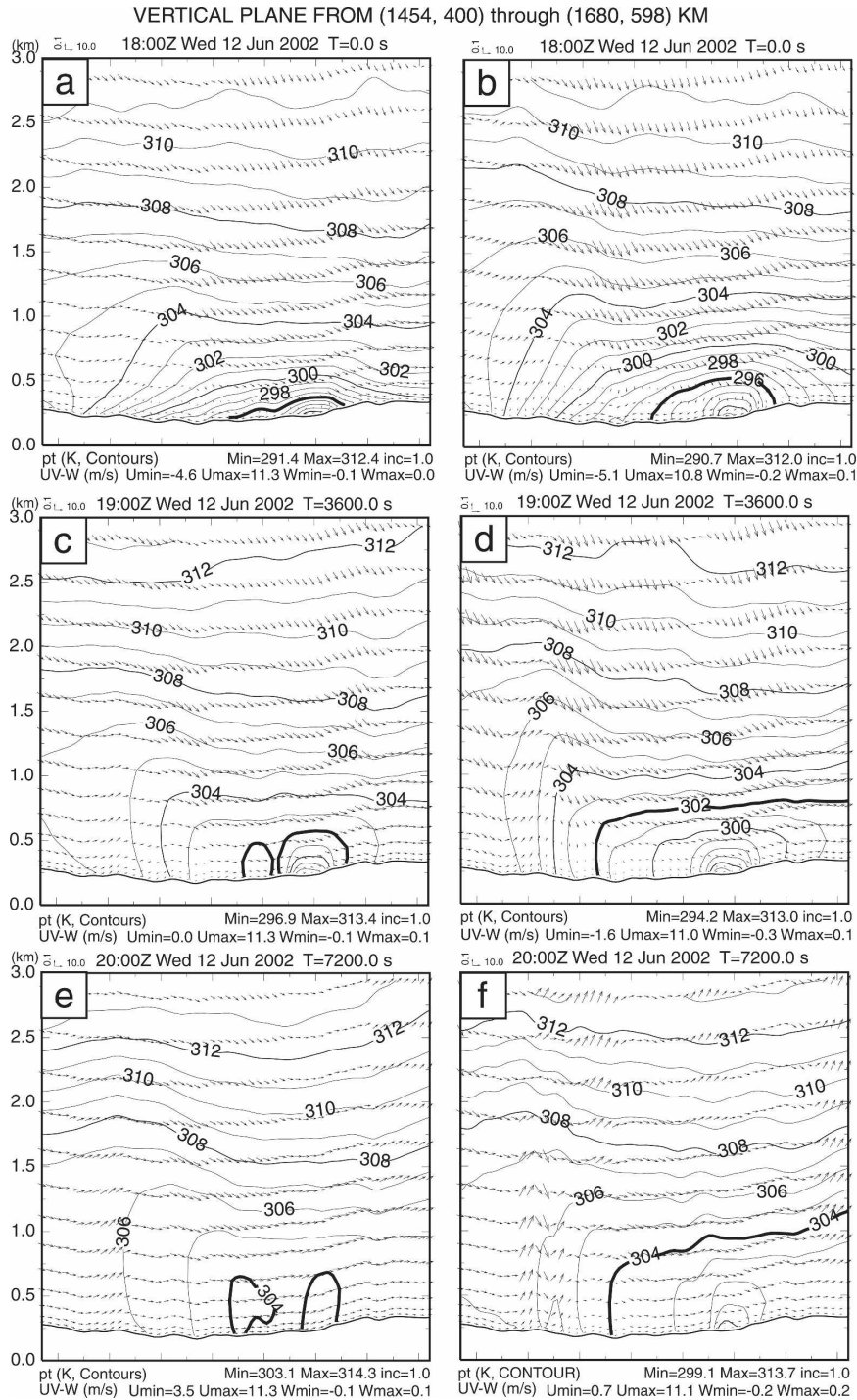


FIG. 11. Vertical cross sections of potential temperature and wind vectors projected to the cross section, through points (1454, 400) km and (1680, 598) km as indicated by the thick straight black line in Fig. 4e, at (top) 1800, (middle) 1900, and (bottom) 2000 UTC for experiments (left) CNTL and (right) ZRANGE. Certain characteristic contours are highlighted as bold to facilitate comparison.

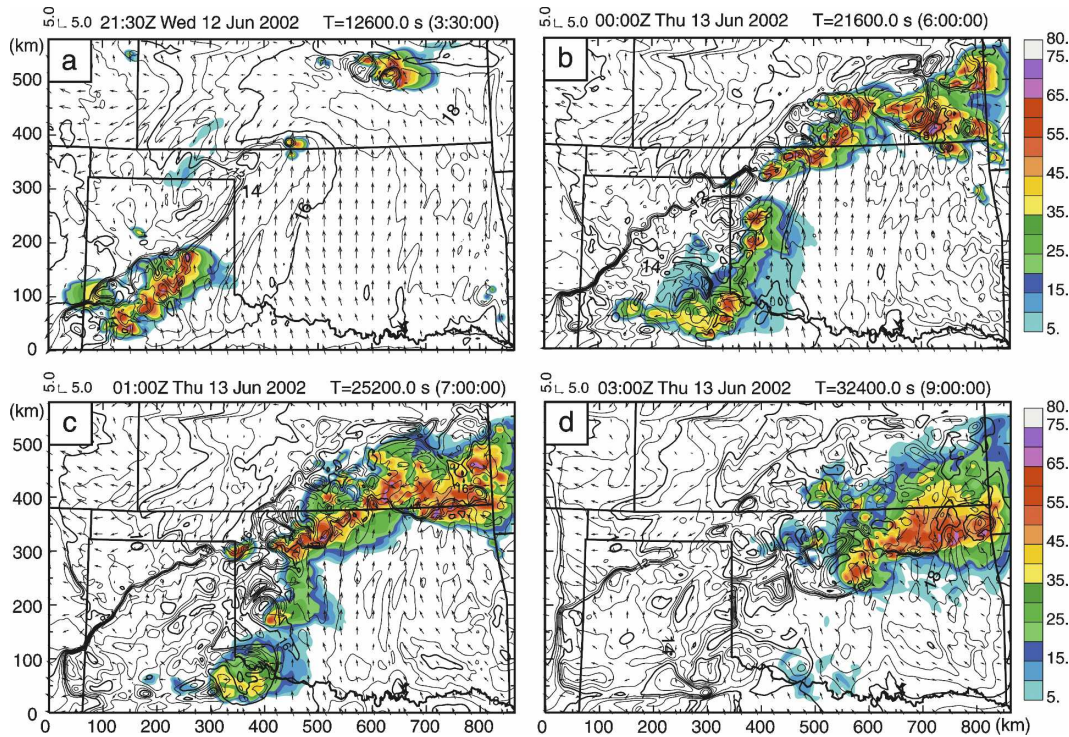


FIG. 12. As in Fig. 6, but for the small-domain experiment SML at (a) 2130 UTC 12 Jun 2002, (b) 0000, (c) 0100, and (d) 0300 UTC 13 Jun 2002.

the flow ahead (east) of the dryline turned from south-southwesterly into south-southeasterly, as a response to the elevated heating and to the tightening mesoscale low circulation in the OK Panhandle (cf. Fig. 4). In our initial experiments, a smaller domain was used, as shown by the box in Fig. 3. With this smaller domain, the western boundary is located just west of the NM–TX border and the southern boundary is about 200 km north of the larger domain boundary. In experiment SML (Table 2), the same configurations, including the assimilation cycles, as CNTL are used, except for the use of this smaller domain (cf. Fig. 1). In this case, the westerly winds behind the dryline are found to be too strong (which mostly came from the lateral boundary condition) compared to the observations (now shown), and the upslope acceleration east of the dryline is too weak, causing the dryline to propagate too far to the east. In fact, the observed low-level winds at the western boundary of SML turned from westerly to easterly shortly after 1800 UTC due to the spreading of cold air behind the southward advancing cold front (cf. Fig. 4d), while in SML the winds at the boundary remained westerly (incorrectly). Consequently, the dryline and the storms along its southern portion propagated too far to the east (Fig. 12). The too weak upslope flow was related to the fact that the southern boundary was located

within the region of flow response. A separate experiment in which the southern boundary alone was placed farther south, to a location similar to that of CNTL, a much stronger upslope response was obtained (not shown). The too strong westerly winds behind the dryline in SML also enhanced the convergence along the dryline, resulting in earlier initiation of cell groups 1a and 2 (Table 2 and Fig. 12a) than in CNTL. The initiation of group 3 was affected by the too far eastward propagation of cell group 2 (Fig. 12b).

To see if the upslope flow was a response to the elevated heating or to the dryline convection, we performed an alternative experiment to CNTL, in which the moist processes were turned off. In that case, the upslope flow response was found to be as strong as in the moist case, suggesting that convective heating did not play a major role.

The location of the eastern boundary of the model also affects our simulations in a significant way, especially in terms of the winds in northeast OK, northwest AR, and southeast KS that are associated with the cold outflow from the MCS passing through that region earlier in that day (see the introduction). When the eastern boundary is located just east of the OK–AR border in SML, a strong southeasterly component of winds through the OK–AR border into the northeastern OK

region is maintained into the later period of simulation (Figs. 12b–d), which actually verified well against OK Mesonet data (not shown). This southeasterly flow is maintained as a result of spreading cold outflow from the MCS in AR and it is apparently captured in the 0000 UTC Eta analysis used to provide the lateral boundary condition. This particular feature is not handled well in all of our experiments that use the larger domain; in fact, a slightly westerly wind component develops early in all the simulations (e.g., Fig. 6) and persists in northeast OK and southeast KS. This problem is clearly related to the fact that the MCS that passed through Kansas in the morning and propagated into Arkansas in the afternoon is not present in the model initial condition (assimilating radar data during the morning hours may help). This deficiency is at least partly responsible for the poor organization of convection at the later stage of forecast in CNTL (Fig. 6) and for the generally northeastward dislocation of convection (cf. Figs. 6d and 2d). Actually, in SML, despite the much poorer evolution of the earlier convection starting from the dryline (which should have mostly dissipated by 0100 UTC anyway, cf. Fig. 2d), the prediction of convective organization into a squall line is actually better reproduced (cf. Figs. 12d, 6d, and 2d). The southeasterly inflow forced in from the eastern boundary against the convective outflow associated with the squall line is believed to have played a role in this.

In most cases, a larger high-resolution domain is preferred. However, in this case, the MCS that passed through southern KS and northeastern OK into AR was not represented in the model; hence, the model, despite its high resolution, was incapable of correctly reproducing the later southeasterly flow. In SML, the use of analysis boundary conditions from Eta helped capture this feature, resulting in a better prediction of convection in this region at the later time.

## 6. Summary

The nonhydrostatic ARPS model with 3-km horizontal resolution is used to numerically simulate the 12–13 June 2002 case from the IHOP\_2002 field experiment that involved initiation of many convective cells along and near a dryline and/or outflow boundary. The ARPS Data Analysis System (ADAS) is used for the data assimilation. The initial condition of the control experiment is generated through hourly intermittent assimilations of routine as well as nonstandard surface and upper-air observations collected during IHOP\_2002 from 1200 to 1800 UTC. The model is then integrated for 9 h, spanning the hour before the first observed

convective initiation along the dryline through the mature stage of a squall line organized from a number of initiated cells. The forecast domain is chosen large enough to minimize any negative effects from the lateral boundary.

As verified against observed reflectivity fields, the model reproduced most of the observed convective cells with reasonably good accuracy in terms of the initiation timing and location, and predicted well the general evolution of convection within the first 7 h of prediction. Detailed characteristics that were captured by the model include cell splitting, merger and regrouping, and the triggering of secondary convective cells by the original MCS outflow boundary colliding with the outflow boundary from dryline convection. The main deficiencies of the prediction are with the organization of cells into a squall line and its propagation, during the last 2 h of the 9-h forecast, and the delay in timing of initiation in most cases.

Sensitivity experiments were performed to examine how the data assimilation intervals and nonstandard observations influence the prediction of convective initiation and evolution. The results show that the experiment with 3-hourly assimilation cycles provides the best CI prediction overall, while the control experiment with hourly assimilation intervals predicts the best convective evolution. The CI in the control experiment is delayed in general. Suggested causes are the insufficient spatial resolution and the typically damping effect on the forced ascent in the high-resolution forecast background when assimilating data that contain only mesoscale information. The apparent improvement to the timing of some of the CI in the experiment that did not include nonstandard data is suggested to be due not necessarily to a better initial condition, but rather to the cancellation of resolution-related delay and the too moist initial condition at the low levels. Indeed, the convection is earlier when 1-km horizontal resolution is used, the results of which will be reported in Part II.

The vertical correlation scales used in ADAS, which employs multipass successive corrections, are shown to significantly impact the structure of the analyzed cold pool using surface observations. Larger vertical correlation scales resulted in a deeper cold pool that lasted longer, leading to stronger convergence and earlier initiation at the outflow boundary. Truly flow-dependent background error covariances will be needed to provide the best information on how the surface observation information should be spread in the vertical.

When the western boundary of the model grid was placed close to the southwest end of the dryline, apparently too strong westerly flow initiated convection at the dryline earlier, and helped push the convective cells

too far to the east. When the southern boundary of the model grid is placed not far enough south, the upslope flow response east of the dryline is constrained significantly, reducing the easterly flow component needed to slow down the eastward propagation of the dryline and related convection. When the eastern boundary is placed near the Oklahoma–Arkansas border in order to bring in observed information of the spreading cold pool from the earlier mesoscale convection in Arkansas, the information helped improve the prediction of flow ahead of an organizing squall line later into the prediction, hence leading to a better organized squall line. We hypothesize that if radar data associated with the MCS are properly assimilated, the MCS outflow can be better predicted and the squall-line organization should be improved. This can be tested in the future.

Preliminary analyses of model results indicate that convection south of the outflow boundary is initiated where low-level localized convergence maxima are found. Boundary layer convective rolls and eddies clearly played important roles, as found in our earlier study (Xue and Martin 2006b), and as suggested by the observation-based study by Weckwerth et al. (2008) on this same case. A more detailed analysis on the initiation mechanisms will be presented in Part II of this paper.

In the end, we point out that the simulation obtained within this study is not perfect. As discussed in section 4, even though the correct prediction of secondary cells triggered by outflow boundary collision is remarkable, there exists a discrepancy between the model simulation and observation with respect to a cell development near the southwest corner of the zoomed-in window (Fig. 6b). The control simulation also did a poor job in producing an organized squall line after 0100 UTC 13 June. The inadequate handling of low-level flows in eastern Oklahoma, ahead of the squall line, is believed to be the main cause. The improved results in a small-domain experiment (SML), where analyzed fields are used as the condition at the domain boundary located near the eastern Oklahoma border, support this belief. It is expected that radar data assimilation that helps better define the MCS and the associated outflow throughout the period will help improve the prediction results. Xiao and Sun (2007) demonstrate, for the same case, that the assimilation of radar data before 0000 UTC 13 June, helps produce a good squall-line forecast after this time. Finally, we also point out that some of the sensitivity results obtained in this paper may be case dependent.

*Acknowledgments.* This work was mainly supported by NSF Grants ATM-0129892 and ATM-0530814. M.

Xue was also supported by NSF Grants ATM-0331756, ATM-0331594, and EEC-0313747, and by grants from the Chinese Academy of Sciences (2004-2-7) and the Chinese Natural Science Foundation (40620120437). Dr. William Martin helped prepare the IHOP data and proofread the manuscript. Jian Zhang and Wenwu Xia of NSSL provided the mosaic reflectivity data and Dr. Ming Hu helped plot the mosaic data. Supercomputers at the Pittsburgh Supercomputing Center were used for most of the experiments.

#### REFERENCES

- Benjamin, S. G., and Coauthors, 2004: An hourly assimilation–forecast cycle: The RUC. *Mon. Wea. Rev.*, **132**, 495–518.
- Bratseth, A. M., 1986: Statistical interpolation by means of successive corrections. *Tellus*, **38A**, 439–447.
- Brewster, K., 1996: Application of a Bratseth analysis scheme including Doppler radar data. Preprints, *15th Conf. on Weather Analysis and Forecasting*, Norfolk, VA, Amer. Meteor. Soc., 92–95.
- Brock, F. V., and S. Fredrickson, 1993: Oklahoma mesonet data quality assurance. Preprints, *Eighth Symp. on Meteorological Observations and Instrumentation*, Anaheim, CA, Amer. Meteor. Soc., 311–316.
- , K. C. Crawford, R. L. Elliott, G. W. Cuperus, S. J. Stadler, H. L. Johnson, and M. D. Eilts, 1995: The Oklahoma Mesonet: A technical overview. *J. Atmos. Oceanic Technol.*, **12**, 5–19.
- Chou, M.-D., 1990: Parameterization for the absorption of solar radiation by O<sub>2</sub> and CO<sub>2</sub> with application to climate studies. *J. Climate*, **3**, 209–217.
- , 1992: A solar radiation model for use in climate studies. *J. Atmos. Sci.*, **49**, 762–772.
- , and M. J. Suarez, 1994: An efficient thermal infrared radiation parameterization for use in general circulation models. NASA Tech. Memo. 104606, 85 pp.
- Dawson, D. T., II, and M. Xue, 2006: Numerical forecasts of the 15–16 June 2002 Southern Plains severe MCS: Impact of mesoscale data and cloud analysis. *Mon. Wea. Rev.*, **134**, 1607–1629.
- Evensen, G., 1994: Sequential data assimilation with a nonlinear quasi-geostrophic model using Monte Carlo methods to forecast error statistics. *J. Geophys. Res.*, **99** (C5), 10 143–10 162.
- Fritsch, J. M., and R. E. Carbone, 2004: Improving quantitative precipitation forecasts in the warm season: A USWRP research and development strategy. *Bull. Amer. Meteor. Soc.*, **85**, 955–965.
- Hu, M., and M. Xue, 2007: Impact of configurations of rapid intermittent assimilation of WSR-88D radar data for the 8 May 2003 Oklahoma City tornadic thunderstorm case. *Mon. Wea. Rev.*, **135**, 507–525.
- Lin, Y.-L., R. D. Farley, and H. D. Orville, 1983: Bulk parameterization of the snow field in a cloud model. *J. Climate Appl. Meteor.*, **22**, 1065–1092.
- Markowski, P., C. Hannon, and E. Rasmussen, 2006: Observations of convection initiation “failure” from the 12 June 2002 IHOP deployment. *Mon. Wea. Rev.*, **134**, 375–405.
- Stano, G., 2003: A case study of convective initiation on 24 May 2002 during the IHOP field experiment. School of Meteorology, University of Oklahoma, 106 pp.

- Stensrud, D. J., and J. M. Fritsch, 1994: Mesoscale convective systems in a weakly forced large-scale environment. Part II: Generation of a mesoscale initial condition. *Mon. Wea. Rev.*, **122**, 2084–2104.
- , G. S. Manikin, E. Rogers, and K. E. Mitchell, 1999: Importance of cold pools to NCEP mesoscale Eta Model forecasts. *Wea. Forecasting*, **14**, 650–670.
- Sun, W.-Y., and C.-Z. Chang, 1986: Diffusion model for a convective layer. Part I: Numerical simulation of convective boundary layer. *J. Climate Appl. Meteor.*, **25**, 1445–1453.
- Warner, T. T., R. A. Peterson, and R. E. Treadon, 1997: A tutorial on lateral boundary conditions as a basic and potentially serious limitation to regional numerical weather prediction. *Bull. Amer. Meteor. Soc.*, **78**, 2599–2617.
- Weckwerth, T. M., and D. B. Parsons, 2006: A review of convection initiation and motivation for IHOP\_2002. *Mon. Wea. Rev.*, **134**, 5–22.
- , and Coauthors, 2004: An overview of the International H<sub>2</sub>O Project (IHOP\_2002) and some preliminary highlights. *Bull. Amer. Meteor. Soc.*, **85**, 253–277.
- , H. V. Murphey, C. Flamant, J. Goldstein, and C. R. Pettet, 2008: An observational study of convective initiation on 12 June 2002 during IHOP\_2002. *Mon. Wea. Rev.*, **136**, 2283–2304.
- Wilson, J. W., and R. D. Roberts, 2006: Summary of convective storm initiation and evolution during IHOP: Observational and modeling perspective. *Mon. Wea. Rev.*, **134**, 23–47.
- Xiao, Q., and J. Sun, 2007: Multiple-radar data assimilation and short-range quantitative precipitation forecasting of a squall line observed during IHOP\_2002. *Mon. Wea. Rev.*, **135**, 3381–3404.
- Xue, M., and W. J. Martin, 2006a: A high-resolution modeling study of the 24 May 2002 case during IHOP. Part I: Numerical simulation and general evolution of the dryline and convection. *Mon. Wea. Rev.*, **134**, 149–171.
- , and —, 2006b: A high-resolution modeling study of the 24 May 2002 case during IHOP. Part II: Horizontal convective rolls and convective initiation. *Mon. Wea. Rev.*, **134**, 172–191.
- , J. Zong, and K. K. Droegemeier, 1996: Parameterization of PBL turbulence in a multi-scale non-hydrostatic model. Preprints, *11th Conf. on Numerical Weather Prediction*, Norfolk, VA, Amer. Meteor. Soc., 363–365.
- , K. K. Droegemeier, and V. Wong, 2000: The Advanced Regional Prediction System (ARPS)—A multiscale nonhydrostatic atmospheric simulation and prediction tool. Part I: Model dynamics and verification. *Meteor. Atmos. Phys.*, **75**, 161–193.
- , and Coauthors, 2001: The Advanced Regional Prediction System (ARPS)—A multiscale nonhydrostatic atmospheric simulation and prediction tool. Part II: Model physics and applications. *Meteor. Atmos. Phys.*, **76**, 143–165.
- , D.-H. Wang, J.-D. Gao, K. Brewster, and K. K. Droegemeier, 2003: The Advanced Regional Prediction System (ARPS), storm-scale numerical weather prediction, and data assimilation. *Meteor. Atmos. Phys.*, **82**, 139–170.
- Zhang, J., K. Howard, and J. J. Gourley, 2005: Constructing three-dimensional multiple-radar reflectivity mosaics: Examples of convective storms and stratiform rain echoes. *J. Atmos. Oceanic Technol.*, **22**, 30–42.